energies

Article

A Study of Two Multi-Element Resonant DC-DC Topologies with Loss Distribution Analyses

Yifeng Wang [1,†], Liang Yang [1,*,†], Fuqiang Han [1,†], Shijie Tu [2] and Weiya Zhang [3]

1 School of Electrical Engineering and Automation, Tianjin University, Tianjin 300072, China; wayif@tju.edu.cn (Y.W.); hanxinyu@tju.edu.cn (F.H.)
2 State Grid Jiangxi Electric Power Company Repair Branch, Nanchang 330000, China; tushijie1991@163.com
3 State Grid Nanjing Power Supply Company, Nanjing 210000, China; zhangweiyatju@126.com
* Correspondence: zyangliang@tju.edu.cn; Tel.: +86-022-2740-1479
† These authors contributed equally to this work.

Received: 17 August 2017; Accepted: 12 September 2017; Published: 13 September 2017

Abstract: In this paper, two multi-element resonant DC-DC converters are analyzed in detail. Since their resonant tanks have multiple resonant components, the converters display different resonant characteristics within different operating frequency ranges. Through appropriate design, both of the two proposed converters successfully lower the conversion losses and, meanwhile, broaden the voltage gain ranges as well: one converter is able to take full usage of the third order harmonic to deliver the active power, and thus the effective utilization rate of the resonant current is elevated; while the another minimizes the entire switching losses for power switching devices by restricting the input impedance angle of the resonant tank. Besides, the loss distribution is analyzed for the purpose of guiding the component design. In the end, two 500 W prototypes are fabricated to test the theoretical analyses. The results demonstrate that the two proposed converters can achieve wide voltage gain with the small frequency deviation, which noticeably contributes to highly efficient conversion. Their peak efficiencies are measured as 95.4% and 95.3%, respectively.

Keywords: resonant DC-DC converter; multi-element; loss distribution; efficiency; soft switching

1. Introduction

Soft-switching resonant DC-DC converters have received persistent focus, and relevant studies, concentrating on the topology morphing, control strategy, parameter design and application background, are still developing.

According to the characteristics of the resonant tanks, the resonant DC-DC converters present a band-pass feature and are able to filter out the high order frequency harmonics. Usually, the resonant current exhibits a nearly sinusoidal waveform. Hence, all the power switching devices, (Metal Oxide Semiconductor field effect transistor (MOSFET) switches and diodes) harvest the desirable soft-switching features, and the switching losses decrease significantly. In addition, the electromagnetic interference (EMI) is restricted as well. Related to the above discussions, the resonant converter characterizes high efficiency, high power density and low EMI, and fits well with the high frequency applications [1–5].

Presently, among all kinds of the resonant DC-DC converters, the inductor-inductor-capacitor (LLC) converter and its derivatives are one of the hottest research topics. Famous for the advantages of simple structure, wide soft-switching range, outstanding voltage regulation performance and high efficiency, the LLC converter is broadly applied in diverse applications, such as battery chargers, renewable and distributed energy generation, and switched mode power supplies. At present, on the basis of the classical LLC topology, considerable research has been implemented concentrating on the optimal parameter design [6–8], advanced control strategy [9,10], current balancing [11], bidirectional power transmission [12,13], high-frequency analysis [14,15], and over-current protection [16,17].

Through these studies, better performances are guaranteed for the LLC converters, compared with other DC-DC converters.

The derivative LLC topology is another topic that attracts much attention. Aiming to broaden the voltage range, to reduce magnetic components, to balance the load current, and to improve the efficiency [18–24], these derivatives modify the topology of conventional LLC circuits. Usually by adding extra components such as power switching devices and passive devices, outstanding resonant characteristics can be realized, and some problems of the traditional LLC have also been solved to a certain degree. The LLC converter and its derivatives belong to three-element resonant DC-DC converters. For these converters, the three resonant elements play a decisive role for the characteristic resonance variables, such as the voltage range, the conversion efficiency and the maximum value of the DC voltage gain. However, due to the very limited degree of freedom, these important variables always present contradictory relationships with each other, therefore, further developments are still necessary for the LLC family.

The shortcomings related to the LLC circuit can be effectively alleviated by the usage of the multi-element resonant converters (MRCs) [25]. MRCs are generally defined as the DC-DC converter whose resonant tank contains at least four passive resonant components. The multiple elements render the MRC more resonant frequency points compared with traditional LLC converters. MRCs often exhibit diverse resonant characteristics at different frequencies, thus possessing stronger adaptability to extensive applications. In [26–28], the MRCs employed the dual-transformer architecture. The auxiliary transformer, controlled by auxiliary switches, only operates under certain conditions for the purposes of high step-up voltage gain and circulating energy suppression. Meanwhile, at the rating state, the auxiliary transformer is disabled and the MRC works as a normal LLC converter. In [29,30], two four-element MRCs are discussed in details. Through proper design, fruitful advantages of load current balancing, switching loss reduction are also obtained. Nevertheless, despite the achievements, the contradiction between the efficiency and the voltage range still exists. The MRCs have to promote the operating frequency to high values for wide voltage gain ranges, which inevitably introduces high-frequency losses. Besides, few of these converters have considered the issues of the effective utilization rate of the resonant current, the switching loss reduction and the over-current protection, which are often of great significance for resonant DC-DC converters. Consequently, the performances of the existing MRCs still need to be improved.

Mainly for the consideration of promoting efficiency and widening the voltage range, this paper proposes two multi-element resonant DC-DC converters. For one proposed topology is able to transfer the fundamental and the third order harmonics synchronously, and thus the effective utilization rate of the resonant current is enhanced. For the other type, all the power switching devices have achieved the turn-on and turn-off soft switching under the rating conditions. The two MRCs obtain widely adjustable voltage gains within narrow frequency ranges, and thereby high efficiencies are ensured. The experiments on two 500 W prototypes indicate that the proposed MRC topologies possess good resonant performances, and the highest efficiencies are 95.4% and 95.3%, respectively.

2. Operating Principle of the Proposed Converter

The proposed dual-capacitor-inductor-transformer (CLT) multi-element resonant converter is shown in Figure 1. Both of the topologies have a similar architecture, which is made up of a half-bridge inverter, a resonant tank and a full-bridge diode rectifier. The resonant tank is comprised of two pairs of resonant capacitors (C_1 and C_2), resonant inductors (L_1 and L_2) and high frequency transformers (T_1 and T_2), thus being marked as the dual-CLT MRC. In each topology, these resonant components are arranged almost identically with each other, except for the connections of the secondary sides of T_1 and T_2. Consequently, they are distinguished as the parallel type and the serial type.

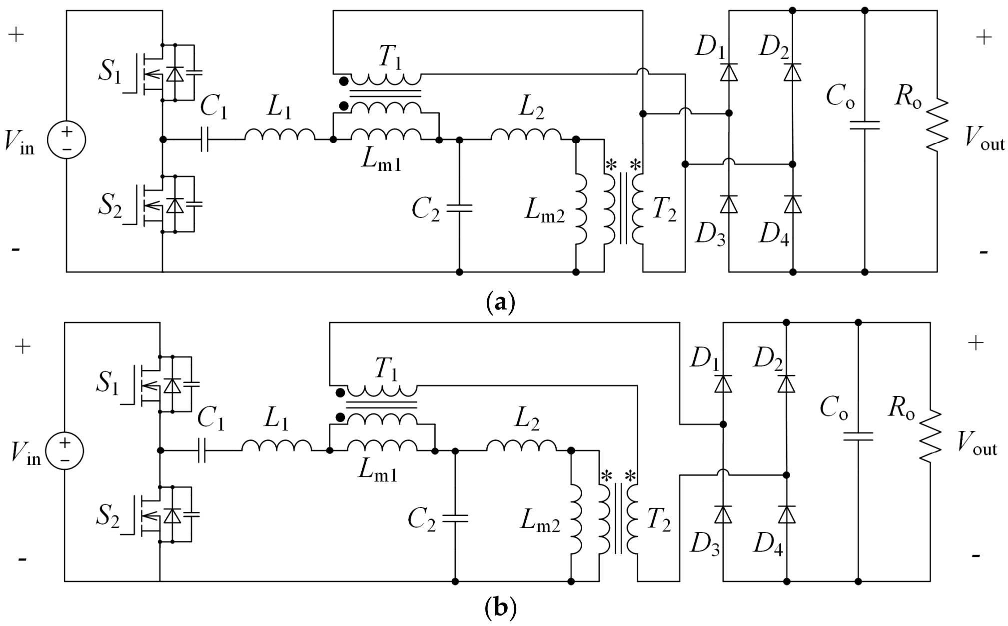

Figure 1. Topology of the MRCs: (**a**) parallel type; (**b**) serial type.

Owing to the multiple elements, these two MRCs have more resonant frequency points, and present diverse resonant characteristics. This feature ensures the proposed topologies hold advantages over the conventional LLC resonant converter. Besides, the side effects caused by the parasitic parameters are also confined from the topology aspect, since the primary-side leakage inductors of T_1 and T_2 are connected in series with L_1 and L_2, respectively. L_1 and L_2 absorb the leakage inductors and participate in the resonance process.

3. Steady-State Analysis

The mathematical models for the two MRCs are established through the first harmonic approximation (FHA) method. Take the parallel type for example to explain the analysis process. The FHA model of the parallel dual-CLT converter is presented in Figure 2. $E_i(s)$ and $E_o(s)$ are the input voltage of the resonant tank and the input voltage of the diode rectifier. $I_1(s)$, $I_2(s)$ and $I_{C2}(s)$ are the currents through L_1, L_2 and capacitor C_2. $I_{s1}(s)$ and $I_{s2}(s)$ are the secondary-side currents.

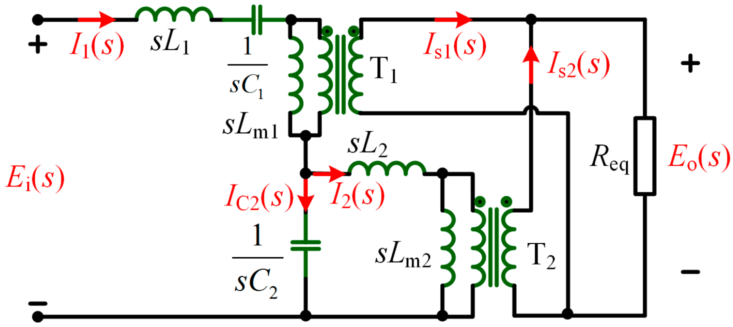

Figure 2. Fundamental harmonic equivalent circuit.

From the Kirchhoff's Laws (current and voltage) such as (1), the expression of the voltage gain M_{pgain} is obtained by Equations (2) and (3). $V_{T1}(s)$, $V_{T2}(s)$ are the primary-side voltages of T_1 and T_2. R_{eq} represents the equivalent ac resistance of the load resistance R_o. A_s, B_s, C_s are intermediate variables.

$$\begin{cases} E_\mathrm{i} = I_1 \cdot (sL_1 + \frac{1}{sC_1}) + V_\mathrm{T1} + I_2 \cdot sL_2 + V_\mathrm{T2} \\ I_\mathrm{C2} \cdot \frac{1}{sC_2} = I_2 \cdot sL_2 + V_\mathrm{T2} \\ I_1 = I_2 + I_\mathrm{C2} \\ V_\mathrm{T1} = N_1 \cdot E_\mathrm{o} \\ V_\mathrm{T2} = N_2 \cdot E_\mathrm{o} \\ I_1 = \frac{V_\mathrm{T1}}{sL_\mathrm{m1}} + \frac{I_\mathrm{S1}}{N_1} \\ I_2 = \frac{V_\mathrm{T2}}{sL_\mathrm{m2}} + \frac{I_\mathrm{S2}}{N_2} \\ E_\mathrm{o} = R_\mathrm{eq} \cdot (I_\mathrm{S1} + I_\mathrm{S2}) \\ R_\mathrm{eq} = \frac{8}{\pi^2} R_\mathrm{o} \end{cases} \tag{1}$$

$$M_\mathrm{pgain} = \left| \frac{V_\mathrm{out}}{V_\mathrm{in}} \right| = \left| \frac{\frac{\pi}{2\sqrt{2}} E_\mathrm{o}}{\frac{\pi}{\sqrt{2}} E_\mathrm{i}} \right| = \left| \frac{1}{2} \frac{1}{A_\mathrm{s} \cdot (\frac{1+R_\mathrm{eq} \cdot B_\mathrm{s}}{R_\mathrm{eq} \cdot C_\mathrm{s}}) + C_\mathrm{s}} \right| \tag{2}$$

$$\begin{cases} A_\mathrm{s} = sL_1 + \frac{1}{sC_1} + \frac{sL_2}{1+s^2C_2L_2} \\ B_\mathrm{s} = \frac{N_1^2}{sL_\mathrm{m1}} + \frac{N_2^2}{sL_\mathrm{m2}} + \frac{sC_2N_2^2}{1+s^2C_2L_2} \\ C_\mathrm{s} = N_1 + \frac{N_2}{1+s^2C_2L_2} \end{cases} \tag{3}$$

Then we substitute $s = j \cdot \omega_\mathrm{s}$ into (2), and M_pgain is modified as in Equations (4) and (5), where $\omega = 2\pi f_\mathrm{op}$ is the angular frequency of the corresponding operating frequency f_op. A_ω, B_ω, C_ω are intermediate variables:

$$M_\mathrm{pgain} = \left| \frac{1}{2} \frac{1}{M_\mathrm{Re} + j \cdot M_\mathrm{Im}} \right| = \left| \frac{1}{2} \frac{1}{(C_\omega + \frac{A_\omega \cdot B_\omega}{C_\omega}) + j \cdot \frac{A_\omega \cdot R_\mathrm{eq}}{C_\omega}} \right| \tag{4}$$

$$\begin{cases} A_\omega = \omega L_1 - \frac{1}{\omega C_1} + \frac{\omega L_2}{1-\omega^2 C_2 L_2} \\ B_\omega = \frac{N_1^2}{\omega L_\mathrm{m1}} + \frac{N_2^2}{\omega L_\mathrm{m2}} - \frac{\omega C_2 N_2^2}{1-\omega^2 C_2 L_2} \\ C_\omega = N_1 + \frac{N_2}{1-\omega^2 C_2 L_2} \end{cases} \tag{5}$$

When the imaginary part M_Im of M_pgain is set to zero, the two resonant points f_p1 and f_p2 can be derived as:

$$\begin{cases} f_\mathrm{p1} = \frac{1}{2\pi} \times \sqrt{\frac{L_1C_1 + L_2C_2 + L_2C_1 - \sqrt{(L_1C_1 + L_2C_2 + L_2C_1)^2 - 4L_1C_1L_2C_2}}{2L_1C_1L_2C_2}} \\ f_\mathrm{p2} = \frac{1}{2\pi} \times \sqrt{\frac{L_1C_1 + L_2C_2 + L_2C_1 + \sqrt{(L_1C_1 + L_2C_2 + L_2C_1)^2 - 4L_1C_1L_2C_2}}{2L_1C_1L_2C_2}} \end{cases} \tag{6}$$

Based on Equations (4) and (5), the gain curves at different loads are drawn in Figure 3. At the resonant points, gain curves are fixed constantly regardless of the load variations, while away from these points, M_pgain will decrease along with the rising load. For the parallel dual-CLT structure, M_pgain reaches the maximum position before f_p1 is reached. After this, it drops at first and then increases near the secondary resonant point f_p2. Beyond f_p2, the voltage gain falls down rapidly to zero and stays at the low values. In particular, it is also seen from the figure that M_pgain drops fast to its half value within a small increase (20%) of the operating frequency f_op from f_p1. Hence, the parallel dual-CLT converter obtains extensively adjustable voltage range without large growth in f_op. For the switches of the inverter, they achieve the desirable turn-on zero voltage switching (ZVS) when f_op is larger than the peak point, and thereby the converter is only allowed to operate within the corresponding scope.

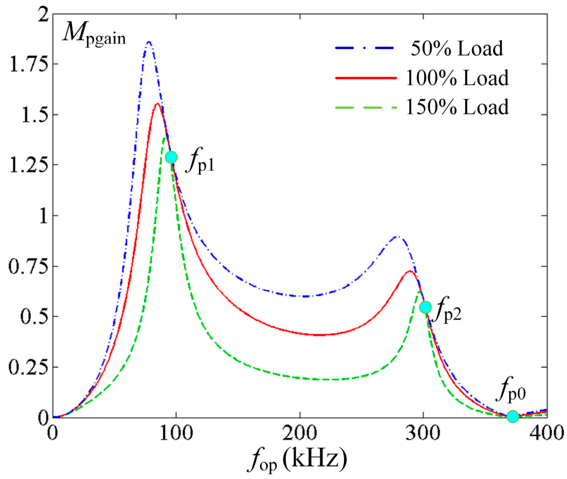

Figure 3. DC voltage gain curves of the parallel dual-CLT converter.

Similarly, the expressions of the voltage gain M_{sgain} and resonant frequency points f_{s1} and f_{s2} are calculated for the serial dual-CLT converter by Equations (7)–(9) and (10) and (11), where $A_{\omega\text{-s}}$, $B_{\omega\text{-s}}$, $C_{\omega\text{-s}}$ are intermediate variables:

$$M_{sgain} = \left| \frac{1}{2} \frac{1}{M_{\text{Re-s}} + j \cdot M_{\text{Im-s}}} \right| \tag{7}$$

$$\begin{cases} M_{\text{Re-s}} = \dfrac{\omega(L_1+L_{m1}) - \frac{1}{\omega C_1} + \frac{\omega(L_2+L_{m2})}{C_{\omega\text{-s}}}}{A_{\omega\text{-s}}} \\ M_{\text{Im-s}} = M_{\text{Re-s}} \cdot \frac{B_{\omega\text{-s}}}{R_{eq}} - \frac{A_{\omega\text{-s}}}{R_{eq}} \end{cases} \tag{8}$$

$$\begin{cases} A_{\omega\text{-s}} = \frac{\omega L_{m1}}{N_1} + \frac{\omega L_{m2}}{N_2} \cdot \frac{1}{C_{\omega\text{-s}}} \\ B_{\omega\text{-s}} = \frac{\omega L_{m1}}{N_1^2} + \frac{\omega L_{m2}}{N_2^2} \cdot \frac{1-\omega^2 C_2 L_2}{C_{\omega\text{-s}}} \\ C_{\omega\text{-s}} = 1 - \omega^2 C_2 (L_2 + L_{m2}) \end{cases} \tag{9}$$

$$f_{s1} = \frac{1}{2\pi} \times \sqrt{\frac{\frac{1}{C_1}\left(\frac{L_{m1}}{N_1^2} + \frac{L_{m2}}{N_2^2}\right)}{(L_1 + L_{m1} + L_2 + L_{m2})\left(\frac{L_{m1}}{N_1^2} + \frac{L_{m2}}{N_2^2}\right) - \left(\frac{L_{m1}}{N_1} + \frac{L_{m2}}{N_2}\right)^2}} \tag{10}$$

$$f_{s2} = \frac{1}{2\pi} \times \sqrt{\frac{(L_1 + L_{m1} + L_2 + L_{m2})\left(\frac{L_{m1}}{N_1^2} + \frac{L_{m2}}{N_2^2}\right) - \left(\frac{L_{m1}}{N_1} + \frac{L_{m2}}{N_2}\right)^2}{C_2\left[\frac{(L_2+L_{m2})L_1 L_{m1}}{N_1^2} + \frac{(L_1+L_{m1})L_2 L_{m2}}{N_2^2}\right]}} \tag{11}$$

We draw in Figure 4 gain curves to reflect the relations of voltage gain versus f_{op} and the load. M_{sgain} curves present similar varying trends as the M_{pgain} curves. However, since the zero resonant point f_{s0} is located in the middle of f_{s1} and f_{s2}, the allowable f_{op} range is restricted within f_{s1} to f_{s0}. M_{sgain} remains zero at f_{s0}, and the serial dual-CLT converter achieves wide gain range from zero to its maximum point in narrow f_{op} range. Besides, f_{s0} also ensures the converter the inherent over-current protection. Since both of the parallel and the serial dual-CLT topologies possess the beneficial wide gain range, they are proved to be competitive for various applications.

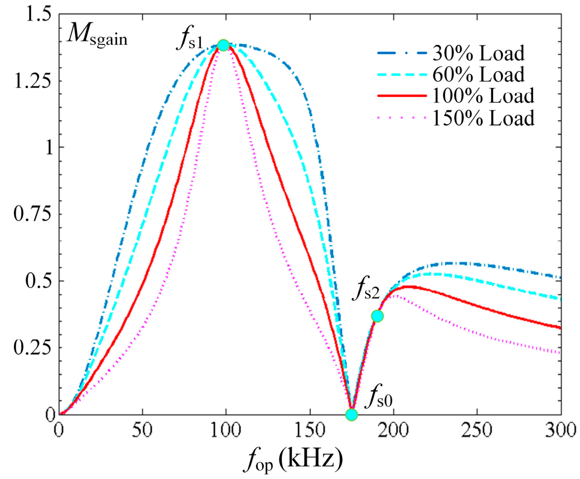

Figure 4. DC voltage gain curves of the serial dual-CLT converter.

4. Parameters Optimization Design

The MRC exhibits different resonant characteristics with different resonant parameters. To pursue the desirable performance, the resonant parameters must be selected. For both of the parallel and the serial dual-CLT MRCs, the main purpose is to obtain high efficiency. However, due to the multiple resonant parameters that have to be designed, massive calculation works must be conducted to find the suitable parameter groups. To alleviate the calculation problem, the MATLAB software (MathWorks, Natick, MA, USA) is recommended to assist with the selection process. The MATLAB program sweeps all the possible resonant parameters and compares them with the pre-set constraints. Then it records the parameters that are in accord with the constraints, while abandoning the other parameters which are inconsistent with. In this approach, the reasonable resonant parameters are chosen. Owing to the difference in topologies, the selection constraints for the two kinds of dual-CLT converters are not same.

4.1. Selection Constraints of the Parallel Topology

Related to the previous discussions, the parallel dual-CLT circuit has two resonant points f_{p1}, f_{p2} and a single zero resonant point f_{p0}. The DC voltage gain M_{pgain} remains constant at these points. It can be seen from Figure 3 that when f_{op} is equal to f_{p1} or f_{p2}, conceptually, the MRCs are able to transfer active power, since their imaginary portions of M_{pgain} reach zero at f_{p1} and f_{p2}. In consequence, if f_{p1} and f_{p2} are arranged deliberately at the first order and the third order harmonic positions, the proposed parallel topology can deliver the 1st and the 3rd active power simultaneously. The utilization of the 3rd order harmonic power will promote the effective utilization rate of the resonant current, which contributes to the high efficiency. The relation between f_{p1} and f_{p2} is shown as:

$$f_{p2} = 3 \times f_{p1} \tag{12}$$

To facilitate the explanation of the utilization rate for the resonant current, the LLC topology is taken for comparison with the proposed parallel dual-CLT converter.

For the conventional LLC converter, the input voltage $e_{LLC}(t)$ of its half-bridge resonant tank is a series of square waveforms. Through Fourier transform, $e_{LLC}(t)$ can be expressed as Equation (13), and thereby the corresponding input resonant current $i_{LLC}(t)$ is obtained as Equation (14). φ_n (n = 1, 3, 5, . . .) is the nth input impedance angle of the nth input impedance Z_n (n = 1, 3, 5, . . .) of the resonant tank:

$$e_{LLC}(t) = \frac{2}{\pi} V_{in} [\sin(\omega t) + \frac{1}{3} \sin(3\omega t) + \ldots + \frac{1}{n} \sin(n\omega t) + \ldots] \tag{13}$$

$$i_{\mathrm{LLC}}(t) = \frac{2V_{\mathrm{in}}}{\pi|Z_1|}\sin(\omega t - \varphi_1) + \frac{2V_{\mathrm{in}}}{3\pi|Z_3|}\sin(3\omega t - \varphi_3) + \ldots + \frac{2V_{\mathrm{in}}}{n\pi|Z_{\mathrm{n}}|}\sin(n\omega t - \varphi_{\mathrm{n}}) + \ldots \tag{14}$$

Then the input power P_{inLLC} of the resonant tank is calculated as:

$$\begin{aligned} P_{\mathrm{inLLC}} &= \tfrac{1}{T_{\mathrm{s}}}\int_0^{T_{\mathrm{s}}} e_{\mathrm{LLC}}(t) i_{\mathrm{LLC}}(t)dt \\ &= \tfrac{1}{T_{\mathrm{s}}}\int_0^{T_{\mathrm{s}}} \sum_{n=1}^{\infty}\sum_{m=1}^{\infty} \tfrac{4V_{\mathrm{in}}^2}{\pi^2|Z_{\mathrm{m}}|nm}\sin(n\omega t)\cdot\sin(m\omega t - \varphi_{\mathrm{m}})dt \end{aligned} \tag{15}$$

Since in one entire period, the integral value will be in close approach to zero if $n \neq m$. Hence, only the integral terms, of which $n = m$, are reserved as shown in Equation (16):

$$P_{\mathrm{inLLC}} = \frac{1}{T_{\mathrm{s}}}\int_0^{T_{\mathrm{s}}} \sum_{n=1}^{\infty} \frac{4V_{\mathrm{in}}^2}{\pi^2|Z_{\mathrm{n}}|}\frac{1}{n^2}\sin(n\omega t)\cdot\sin(n\omega t - \varphi_{\mathrm{n}})dt \tag{16}$$

Related to the resonant characteristic of the LLC topology [6–8], the DC voltage gain maintains high values when f_{op} is near the resonant point, while the gain curves are confined progressively for the high order harmonics. As a result, the input impedances Z_{n} for $n \geq 3$ cases are very large, and they force the corresponding integral terms near zero. Equation (16) is expressed approximately as Equation (17), where only the fundamental component of $i_{\mathrm{LLC}}(t)$ is used to transfer the active power:

$$P_{\mathrm{inLLC}} = \frac{1}{T_{\mathrm{s}}}\int_0^{T_{\mathrm{s}}} \frac{4V_{\mathrm{in}}^2}{\pi^2|Z_1|}\sin(\omega t)\cdot\sin(\omega t - \varphi_1)dt \tag{17}$$

For the proposed parallel dual-CLT converter, the similar Fourier transform is also applied to express the input voltage $e_{\mathrm{CLT}}(t)$ and the input resonant current $i_{\mathrm{CLT}}(t)$ of the resonant tank. Then the input power P_{inCLT} is calculated as Equation (18). Different from the LLC topology, the proposed converter possesses two resonant points, which are arranged as Equation (12). Therefore, both of the input impedances Z_1 and Z_3 are much smaller than higher order impedances. Neglecting the high order terms ($n \geq 5$), Equation (17) is transformed into Equation (18):

$$P_{\mathrm{inCLT}} = \frac{1}{T_{\mathrm{s}}}\int_0^{T_{\mathrm{s}}} \frac{4V_{\mathrm{in}}^2}{\pi^2|Z_1|}\sin(\omega t)\cdot\sin(\omega t - \varphi_{\mathrm{n}}) + \frac{4V_{\mathrm{in}}^2}{9\pi^2|Z_1|}\sin(3\omega t)\cdot\sin(3\omega t - \varphi_3)dt \tag{18}$$

It is clearly seen that P_{inCLT} contains the 1st and 3rd terms, which infers the proposed parallel dual-CLT converter is able to transfer the first and the third harmonic active power simultaneously. Compared with Equation (16), the extra 3rd term helps to improve the utilization rate of the resonant current, which will lead to highly efficient conversion.

Then from Equations (4)–(6), the MATLAB program sweeps the possible resonant parameter ranges, and records the satisfactory parameter groups. Through observation, these recorded parameters can be classified into two types according to the size relationship of the voltage gains at f_{p1} and f_{p2}. Figure 5 shows the resonant waveforms for the two parameter types. For Type I, the gain curves in Figure 5a indicate $M_{\mathrm{pgain}}(f_{\mathrm{p1}})$ is smaller than $M_{\mathrm{pgain}}(f_{\mathrm{p2}})$, and hence the 3rd component evidently takes a large share of the resonant current. Even, with certain Type-I groups, the proportion of 3rd component exceeds that of the 1st component, and the resonant current will flow negatively during the positive half switching cycle as Figure 5c presents. Meanwhile, for Type II, $M_{\mathrm{pgain}}(f_{\mathrm{p1}})$ is larger than $M_{\mathrm{pgain}}(f_{\mathrm{p2}})$ in Figure 5b, and 1st component domains the resonant current as presented in Figure 5d.

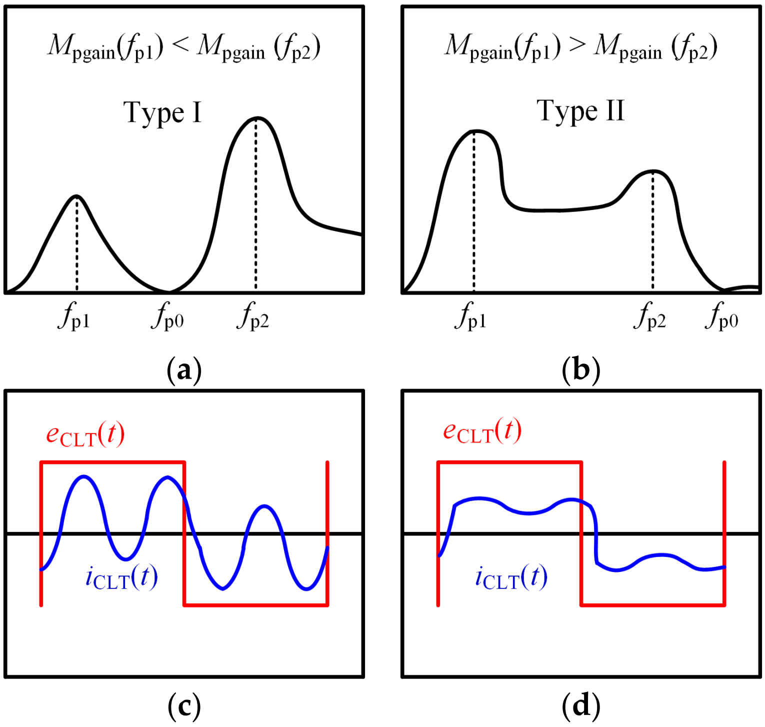

Figure 5. Voltage gain curves and main waveforms of the two type parameters: (**a**) gain curve of Type I; (**b**) gain curve of Type II; (**c**) resonant waveforms of Type I; (**d**) resonant waveforms of Type II.

Although both of the two types successfully deliver the third harmonic active power, Type II has distinct advantages over Type I. For one thing, higher order switching losses are introduced into the switching devices since the 3rd component takes up a large share in Type I. For another, the larger proportion of high frequency ingredient also aggravates the skin effects. The skin depth of the 3rd component is smaller than that of the 1st component, resulting in larger ac resistance and higher conduction losses. Concerning this aspect, the constraint of $M_{pgain}(f_{p1}) > M_{pgain}(f_{p2})$ should be also included in the MATLAB program.

For a pre-set application, the input and output voltage levels must be designed properly. In this paper, the rated input voltage V_{in} is set at 400 V and the rated output voltage V_{out} is set at 52 V. The corresponding rating DC voltage gain M_{pgain} is calculated as 0.13.

Comprehensively considering the aforementioned analyses, the flow chart of the MATLAB program is presented in Figure 6.

In the final step, the voltage stresses of the resonant capacitors are taken into account, since they directly determine the selection of these capacitors. Generally speaking, capacitors with higher withstand voltages are often more expensive than their low-value counterparts. So, for cost issue, the parameter group with the minimum voltage stresses is chosen as the final optimization result.

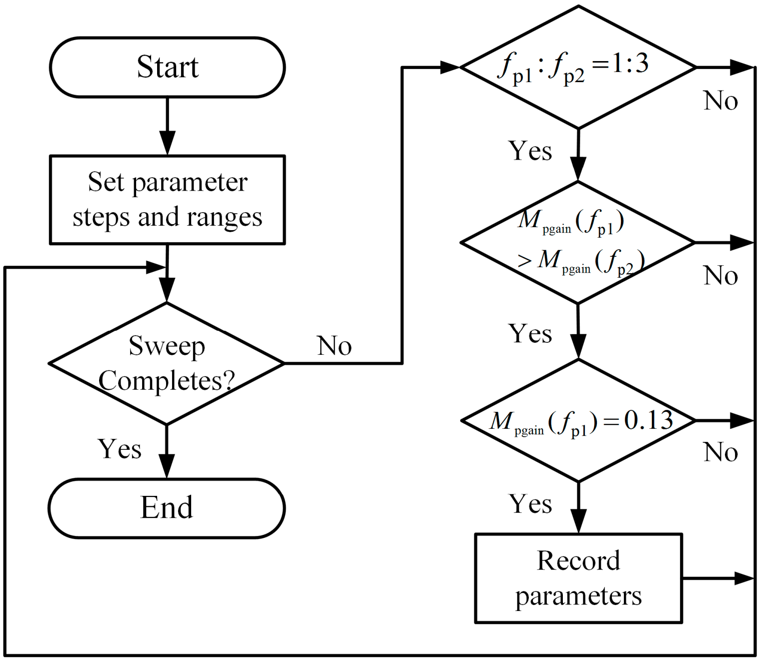

Figure 6. Flow chart of the MATLAB program for the parallel converter.

4.2. Selection Constraints of the Serial Topology

The design process of the resonant parameters for the serial dual-CLT converter is basically similar with that of the parallel converter. From Figure 4, the selection constraints are listed as the followings.

(a) $f_{s1} < f_{s0} < f_{s2}$. According to Equations (10) and (11), the three resonant points should be set as this inequation, so that the gain curve is consistent with Figure 4. Since the ZVS region is from f_{s1} to f_{s0}, the serial converter obtains widely adjustable gain range within this scope.

(b) f_{s1} = 100 kHz. The rated operating frequency should be set closely enough to the resonant point f_{s1}, and thereby f_{s1} is set at 100 kHz here.

(c) f_{s0} = 180 kHz. $M_{sgain}(f_{s0})$ stays at zero theoretically and contributes to wide voltage gain range starting from zero. If f_{s0} is far away from f_{s1}, the converter must increase the operating frequency significantly to achieve wide gain range, which will inevitably introduce high frequency losses. Meanwhile, when f_{s0} is too close to f_{s1}, then the circulating energy will be enhanced as the following outcomes, since the input impedance angle is elevated dramatically. In this case, f_{s0} is set at 180 kHz as the compromise result.

(d) $M_{sgain}(f_{s1})$ = 0.13. Same with the parallel dual-CLT converter, the rating input and output voltages are also set at 400 V and 52 V.

The flow chart of the MATLAB program is presented in Figure 7. Also concerning the voltage stresses of the resonant capacitors, the parameters for the serial dual-CLT converter are chosen finally.

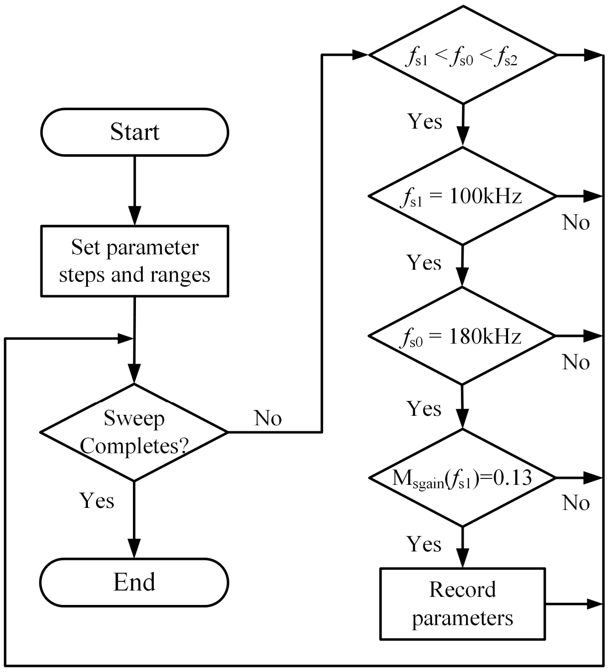

Figure 7. Flow chart of the MATLAB program for the serial converter.

The selected parameters are listed in Table 1. The following loss distribution analyses and the experiments are conducted based on these parameters.

Table 1. Parameters of the MRCs.

Converter Parameter	Parallel Structure	Serial Structure
Resonant Inductor L_1	190 µH	100 µH
Resonant Inductor L_2	25 µH	50 µH
Resonant Capacitor C_1	13 nF	15 nF
Resonant Capacitor C_2	13 nF	3 nF
Magnetizing Inductor of T_1 L_{m1}	200 µH	550 µH
Turns Ratio of T_1 N_1	2	4.5
Magnetizing Inductor of T_2 L_{m2}	200 µH	650 µH
Turns Ratio of T_2 N_2	1.5	3.5

5. Loss Distribution Analyses

After the optimal resonant parameters are designed, in the next step, power devices, including the magnetic components, MOSFET switches and diodes, are going to be chosen and fabricated. However, limited by the craftsmanship, power devices even with the totally identical values may have significant deviations with each other, which deteriorates the efficiency of the MRCs. Since the efficiency issue is tightly relevant with the fabrication of power devices, the loss distribution of these devices should be studied to estimate the conversion efficiency and to guide the fabrication.

Generally, the dominant ingredients of the total power losses for a resonant DC-DC converter contain the losses of power switches, losses of diodes, losses of magnetic components (transformers and inductors) and other losses. In this section, also taking the parallel dual-CLT converter for instance, these losses are analyzed in detail.

5.1. Transformer Losses

For a transformer, the main losses are made up of the conduction loss and the magnetic loss. The conduction loss is produced when the resonant currents flow through the primary- and secondary-side copper coils of the high frequency transformers. $R_{\text{T1-pri}}$ represents the primary-side DC conduction resistance of transformer T_1, and is calculated as:

$$R_{\text{T1-pri}} = \rho_{\text{Cu}} \frac{l_{\text{T1}}}{S_{\text{Cu}}} \tag{19}$$

where ρ_{Cu} is the electric resistivity of the copper wire, l_{T1} is the length of the conductor and can be calculated by the winding geometry, S_{Cu} is the equivalent sectional area of the wires. Under the high-frequency condition, the skin effect forces the conducting currents approaching to the surfaces of the conductors, which will make the ac conduction resistance $R_{\text{T1-pri-ac}}$ larger than $R_{\text{T1-pri}}$. Hence, through the Dowell's equation, the AC-to-DC resistance ratio $K_{\text{T1-ad}}$ of the nth harmonic is calculated as Equation (20). In this case, only the 1st and 3rd harmonics are concerned, while higher order components are neglected due to their small values:

$$K_{\text{T1-ad}} = M_{\text{T1}} \cdot \frac{\sinh(2M_{\text{T1}}) + \sin(2M_{\text{T1}})}{\cosh(2M_{\text{T1}}) - \cos(2M_{\text{T1}})} + 2M_{\text{T1}} \cdot \frac{n_{\text{lay}}^2 - 1}{3} \cdot \frac{\sinh(2M_{\text{T1}}) - \sin(2M_{\text{T1}})}{\cosh(2M_{\text{T1}}) + \cos(2M_{\text{T1}})} \tag{20}$$

where n_{lay} is the layers of the primary-side windings of T_1, M_{T1} is the intermediate variable combining the skin depth δ_{n} and the diameter d_{wire} of the copper wire. The nth δ_{n} is calculated as (21), and f_{op}, μ_0 are the operating frequency and the vacuum permeability:

$$\delta_{\text{n}} = \sqrt{\frac{\rho_{\text{Cu}}}{\pi n f_{\text{op}} \mu_0}} \tag{21}$$

The primary-side conduction loss is expressed as Equation (22), and $I_1(n)$ is the root-mean-square (RMS) value of the nth primary-side resonant current:

$$P_{\text{T1-con-pri}} = R_{\text{T1-pri}} \sum_{n=1}^{3} K_{\text{T1-ad}}(n) I_1^2(n) \tag{22}$$

The secondary-side conduction $P_{\text{T1-con-sec}}$ loss can be obtained as well according to Equations (19)–(22). A copper foil is used to substitute the Litz wires in the secondary side, so $n_{\text{lay}} = N_{\text{T1sec}}/2$ and $M_{\text{T1}} = H_{\text{foil}}/\delta_{\text{n}}$ at this situation, where N_{T1sec} is the turns of the secondary-side windings and H_{foil} is the height of the foil.

The Steinmetz equation is applied to estimate the core loss $P_{\text{T1-mag}}$ as Equation (23). V_{core} is the volume of the magnetic core, ΔB_{T1} is the flux swing, k, α_{core}, β_{core} are the Steinmetz coefficients which are provided by the manufacturer. For ΔB_{T1}, it is calculated as Equation (24), where N_{T1pri} is the turns of the primary-side windings, v_{T1} is the primary-side voltage of T_1, A_{core} is the equivalent sectional area of the magnetic core, T_{s} is the switching period:

$$P_{\text{T1-mag}} = V_{\text{core}} \cdot k f_{\text{op}}^{\alpha_{\text{core}}} \Delta B_{\text{T1}}^{\beta_{\text{core}}} \tag{23}$$

$$\Delta B_{\text{T1}} = \frac{\int_0^{\frac{T_{\text{s}}}{2}} |v_{\text{T1}}| dt}{N_{\text{T1pri}} A_{\text{core}}} \tag{24}$$

The total losses of T_1 is calculated as:

$$P_{\text{T1}} = P_{\text{T1-con-pri}} + P_{\text{T1-con-sec}} + P_{\text{T1-mag}} \tag{25}$$

Similarly, the losses P_{T2} of T_2 can be obtained based as well.

5.2. Inductor Losses

The estimation of the inductor losses is basically same with that of the transformers. The conduction losses P_{L1con}, P_{L2con} of L_1 and L_2 are achieved through Equations (19)–(22) too. The core losses P_{L1mag},

P_{L2mag} are estimated by the Steinmetz equations as (23). In addition, for L_1, the flux swing ΔB_{L1} is calculated as Equation (26), and $I_{L1\text{-max}}$ is the peak current of L_1, N_{L1} is the winding turns:

$$\Delta B_{L1} = \frac{L_1 I_{L1\text{-max}}}{N_{T1pri} A_{core}} \tag{26}$$

Then the losses of inductors are attained as:

$$P_{L1} + P_{L2} = P_{L1con} + P_{L1mag} + P_{L2con} + P_{L2mag} \tag{27}$$

5.3. Power Switch Losses

The losses of power switches mainly comprise the switching loss, conduction loss and the drive loss. Since the proposed converter operates at the ZVS state, the turn-on switching loss is restrained greatly, and accordingly this part of loss is neglected for simplification. $I_{turnoff}$ is the turn-off current of the power switch, and can be obtained mathematically or experimentally. Then the turn-off loss is calculated using Equation (28):

$$P_{switching} \approx P_{turnoff} = \frac{f_{op} I_{turnoff} V_{in}}{2} \cdot \left[\frac{Q_{GD} R_G}{V_{pl}} + \frac{2Q_{GS}(R_G + R_{S1})}{V_{pl} + V_{th}}\right] \tag{28}$$

$P_{switching}$ represents the switching loss of S_1. Q_{GD}, Q_{GS} are the storage charges between the gate and drain, the gate and source respectively. V_{pl} is the Miller platform voltage, and V_{th} is the gate threshold voltage. R_G is the equivalent gate impedance and R_{s1} is the serial equivalent impedance of the source port. These parameters can be found in the datasheet of the MOSFET.

The drive loss P_{dri} is calculated as Equation (29), where V_{GD} is the voltage of the power switches:

$$P_{dri} = Q_{GD} V_{GD} f_{op} \tag{29}$$

The conduction loss is deduced as (30), and R_{sw} is the conduction resistance of the power switches:

$$P_{sw\text{-}con} = R_{sw} \sum_{n=1}^{3} I_1^2(n) \tag{30}$$

Consequently, the switch loss P_{SW} is:

$$P_{sw} = 2 \times (P_{switching} + P_{dri} + P_{sw\text{-}con}) \tag{31}$$

5.4. Diode Losses

The diode losses only contain the conduction loss and the switching loss. Whereas, in this topology, these diodes not only achieve the inherent zero-current-switching (ZCS) turn-off soft-switching, but present the quasi-ZCS turn-on characteristic as well, which are proven by experiments in Section 6. Hence, the switching losses of the diode bridge is very small and can be neglected. The relation between the total diode loss P_{diode} and the conduction loss $P_{d\text{-}con}$ of a single diode can be expressed as:

$$P_{diode} \approx 4 \times P_{d\text{-}con} \tag{32}$$

6. Experiments

To verify the feasibility of the proposed dual-CLT MRCs and the reliability of the theoretical analyses, experiments on both of the two MRCs are implemented and compared. Related to the aforementioned analyses, the types and specifications of the power devices are listed in Table 2.

Table 2. Types and specifications of the power devices.

Converter Parameter	Parallel Structure	Serial Structure
Resonant Inductor L_1	PQ3230 PC95	PQ3220 PC95
Resonant Inductor L_2	PQ3230 PC95	PQ2625 PC95
Resonant Capacitor C_1	WIMA 10 nF + 3 × 1 nF	WIMA 10 nF × 6 (Combination)
Resonant Capacitor C_2	WIMA 10 nF + 3 × 1 nF	WIMA 1 nF × 3
Transformer T_1	PQ3230 PC95	PQ3535 PC95
Transformer T_2	PQ3535 PC95	PQ3535 PC95
Power Switch S_1-S_2	C3M0065090D	C3M0065090D
Diode D_1-D_4	DSSK40-008B	DSSK40-008B

In Figure 8, the experimental waveforms of the resonant tanks of the parallel and serial dual-CLT converters are presented. Their prototypes are both tested under the rated conditions. The rated input voltage is 400 V and the output voltage is around 52 V for both topologies (51.6 V for the parallel type and 52.2 V for the serial type). For simplification, the symmetrical variables of the two MRCs are denoted by the same variable symbol. s_1, v_{S1} and i_{S1} represent the drive signal, voltage and current of switch S_1, respectively.

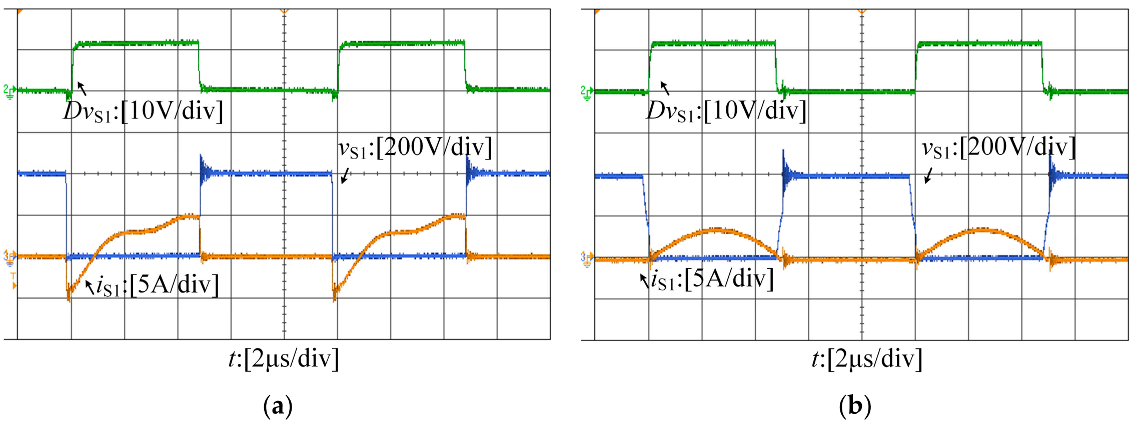

Figure 8. Main waveforms of the resonant tanks: (**a**) parallel type; (**b**) serial type.

In Figure 8a, the main waveforms of the parallel dual-CLT converter are shown. The operating frequency is 100 kHz. i_{S1} lags behind v_{S1}, and thereby the ZVS feature is achieved by the switches. Besides, it is clearly seen that the resonant current i_{S1} exhibits a saddle-shape waveform, since the fundamental and the third harmonic components both exist in i_{S1}. According to the previous analyses, the effective utilization rate of the resonant current is promoted, which contributes to high efficiency. The rating efficiency of the parallel topology is measured as 94.5%.

Figure 9a presents the loss distribution of the parallel converter at the rated situation. The diode loss, the transformer loss and the inductor loss are the main parts of the total losses. Because the proposed converter works under the high step-down condition, the output current is relatively large at the same power level. As a result, the conduction losses of the diode bridge are considerable. The magnetic losses (transformers and inductors) are also the magnificent loss sources. For a single magnetic component, each of the transformers and the inductors only produces limited power losses, but in the proposed converter there are totally four magnetic components in the resonant tank. In consequence, the total magnetic losses cannot be ignored.

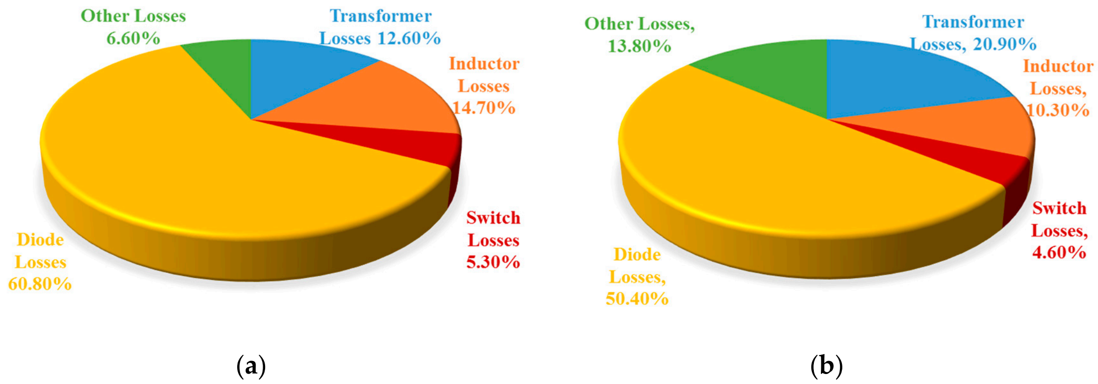

Figure 9. Loss distributions of the rating conditions: (**a**) parallel type; (**b**) serial type.

Figure 8b gives the resonant waveforms of the serial dual-CLT circuit. The switches also guarantee themselves the ZVS turning on. Although this converter fails to take full use of the higher order harmonics, the rating input impedance angle of the resonant tank is designed at a very small level. Consequently, at the turn-off moment, current i_{S1} resonates to almost zero spontaneously, and the turn-off current is constrained greatly. In this case, the small turn-off loss can be overlooked and marked as the quasi-ZCS turning off. Since both of the switching periods of the switches are working in the soft-switching or quasi-soft-switching modes, the switching losses of the power switches in the serial topology reduce to the minimum. The measured rating efficiency is 94.4%.

In Figure 9b, the loss distribution of the serial converter is shown. The diode losses and the magnetic losses also take up large share of the total losses. In particular, the proportion of the switch loss decreases, for the switching losses are confined. The other losses mainly include the capacitor losses, the printed circuit board (PCB) losses and the in/out copper wire losses.

In future work, to further elevate the conversion efficiency, two improvements should be implemented. For one thing, to restrain the large diode conduction loss, the synchronous rectifier (SR) should be employed. With the much lower conduction resistance of the MOSFET switches, the SR contributes significantly to the high efficiency. For another, the magnetic integration technology should also be applied here, while maintaining the desirable resonant characteristics at the same time. By this means, the magnetic losses will be restricted. Theoretically, through the ideal mathematical estimation, the efficiency of the enhanced MRC is going to be as high as over 98%.

Based on the rated 400 V input voltage, the waveforms at different operating frequencies are recorded in Figures 10 and 11 for the two MRCs. For the parallel dual-CLT topology, Figure 10a presents v_{S1}, i_{S1} and the voltage v_{D1} and current i_{D1} of the diode D_1 at 120 kHz. The output voltage V_{out} reduces to 28.5 V along with the f_{op} deviating from the rating point. The input impedance angle increases. At this time, the converter loses the ability to transfer the 3rd harmonic active power, but still realizes the ZVS turning on for switches. The diodes achieve not only the inherent ZCS turning off, but also the quasi-ZCS turn-on feature, since the turn-on current approaches to zero almost. Consequently, the total switching losses of the converter are greatly reduced, and only the turn-off losses of the switches have to be concerned during the loss distribution analyses.

Same conclusions are drawn from Figure 10b,c, where v_{S1}, i_{S1}, v_{D1}, i_{D1} of the parallel structure are also presented. The measured output voltages are 20.3 V and 16.7 V at 150 kHz and 200 kHz, respectively. The switches maintain the ZVS turn-on characteristic, while the diodes realize soft switching for all the turn-on and turn-off processes. Besides, the output voltage at 150 kHz is only 39% of that at the rating state, which indicates the designed circuit is able to provide extensively adjustable voltage gain range within a narrow f_{op} range.

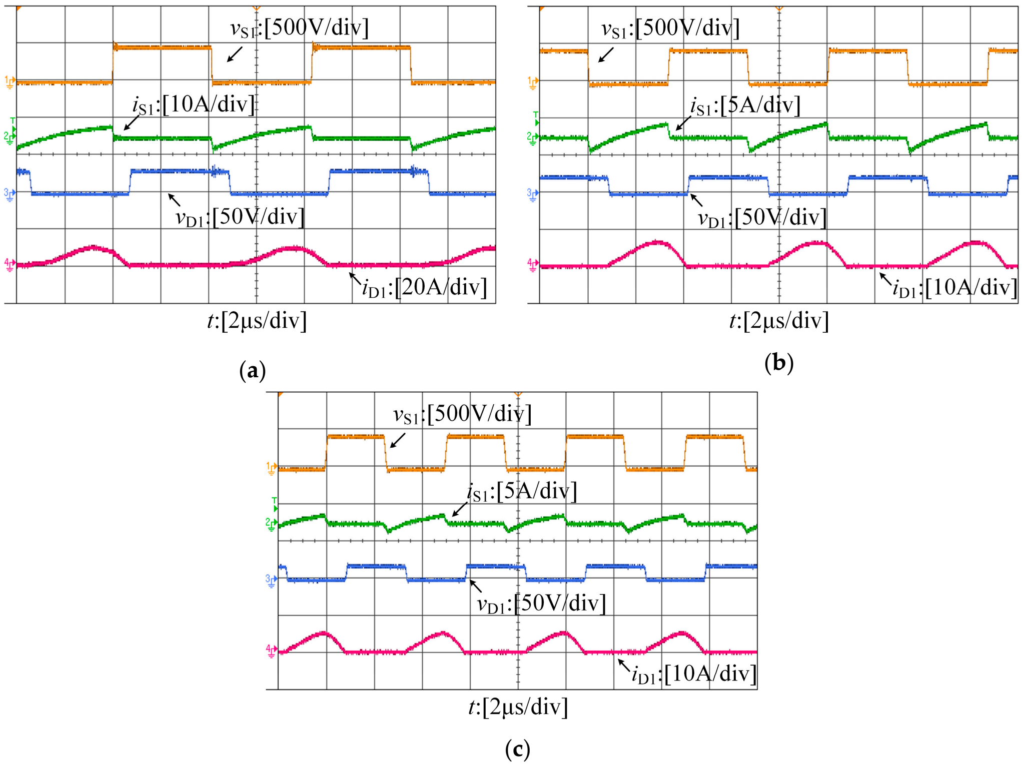

Figure 10. Waveforms at different operating frequencies of the parallel converter: (**a**) 120 kHz; (**b**) 150 kHz; (**c**) 200 kHz.

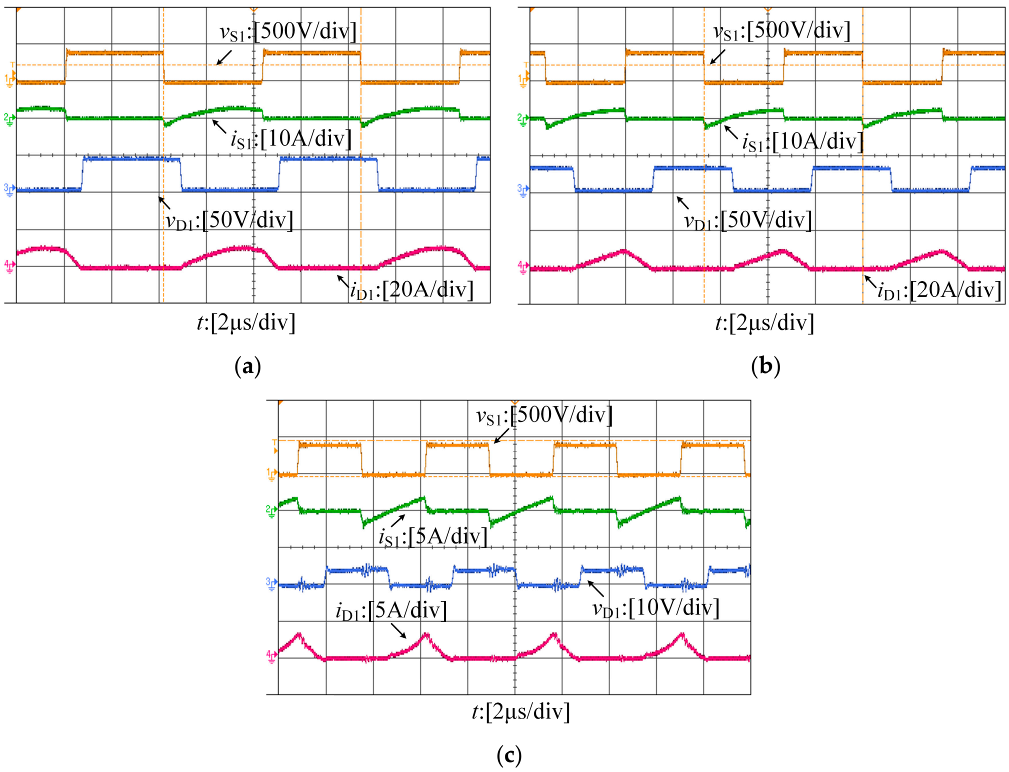

Figure 11. Waveforms at different operating frequencies of the serial converter: (**a**) 120 kHz; (**b**) 150 kHz; (**c**) 176 kHz ($f_{op} \approx f_{s0}$).

By comparison, v_{S1}, i_{S1} v_{D1}, i_{D1} of the serial dual-CLT topology are also tested and shown in Figure 11a–c. The three sub-figures correspond to the operating frequencies of 120, 150 and 176 kHz. Similar with the parallel architecture, the switching losses of the serial-type converter are also restricted due to the soft-switching operations. Wide voltage gain range is obtained, since the output voltage is less than 28.7 V at 150 kHz. Besides, compared to the parallel structure, the serial converter further expands the voltage gain range because of the existing of the zero frequency point f_{s0}. In Figure 11c, when f_{op} equals to 176 kHz, the output voltage is only 3.6 V with the rating input voltage of 400 V, and the corresponding voltage gain M_{sgain} is less than 0.01. This point is regarded as f_{s0} of the serial dual-CLT converter.

In the end, the efficiency curves of the two MRCs are measured at different loads and output voltages as presented in Figure 12. Besides, by comparison, the efficiencies of the LLC converter are also given. Corresponding to Figure 12a–c, the output voltages are 52, 40 and 30 V, respectively. Figure 12a indicates that all the three curves basically coincide with each other at 52 V output, because at this time their operating frequencies are near the rating frequency points and the advantages of the proposed MRCs are not obvious. However, when f_{op} is away from the rating state, the efficiencies of the two MRCs are similar, and they are both higher than the curve of the classical LLC converter. This is because the LLC converter has to increase f_{op} greatly to lower down the voltage gain, which will apparently bring in high-frequency losses and sacrifice efficiency. Figure 12 demonstrates that the proposed MRCs are able to regulate the voltage gain in wide range with only a small frequency deviation. For the parallel and the serial converters, the peak efficiencies are 95.4% and 95.3% at 300 W and 52 V output.

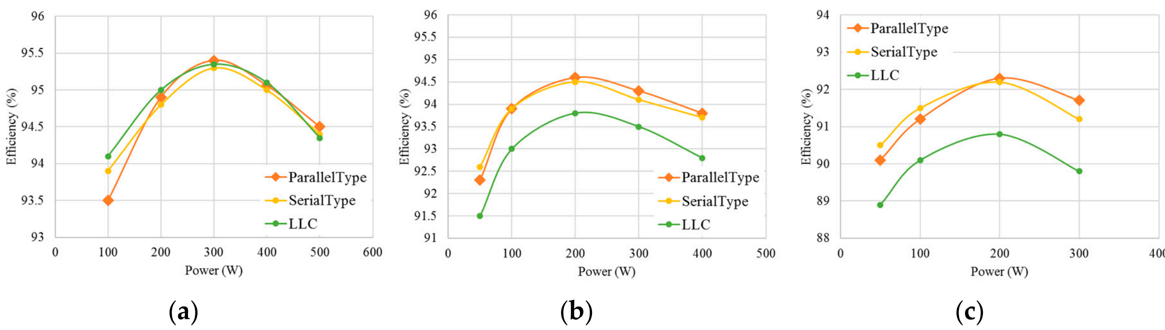

Figure 12. Efficiency curves: (**a**) V_{out} = 52 V; (**b**) V_{out} = 40 V; (**c**) V_{out} = 30 V.

7. Conclusions

Two multi-element resonant DC-DC converters are proposed in this paper. The parallel converter transfers the 1st and 3rd harmonic active power synchronously at the rated condition, and promotes the effective utilization rate. In the serial converter, the switches and diodes achieve the soft switching for all the turn-on and turn-off transitions at rated. Besides, the potential high-frequency losses are avoided, since both MRCs achieve widely adjustable voltage gains within limited frequency ranges. To test the feasibility of the theoretical analyses, two prototypes are implemented at 500 W. The experimental results indicate that both of the two MRCs can ensure high efficiencies among wide load and output voltage scopes. The peak efficiencies are 95.4% and 95.3%, respectively.

Acknowledgments: This research was supported by the National High Technology Research and Development Program of China (863 Program) (Grant: 2015AA050603). The authors also would like to thank the anonymous reviewers for their valuable comments and suggestions to improve the quality of the paper.

Author Contributions: Yifeng Wang and Liang Yang, designed the main parts of the study, including the circuit simulation model, topology innovation and simulation development. Fuqiang Han, Shijie Tu and Weiya Zhang helped in the hardware development and experiment.

Conflicts of Interest: The authors declare no conflict of interest.

References

1. Li, H.Y.; Li, X.; Lu, M.; Hu, S. A linearized large signal model of an LCL-type resonant converter. *Energies* **2015**, *8*, 1848–1864. [CrossRef]
2. Wang, C.S.; Li, W.; Wang, Y.F.; Chen, B. A high-efficiency isolated LCLC multi-resonant three-port bidirectional DC-DC converter. *Energies* **2017**, *10*, 934. [CrossRef]
3. Deng, J.; Li, S.; Hu, S.; Mi, C.C.; Ma, R. Design methodology of LLC resonant converters for electric vehicle battery chargers. *IEEE Trans. Veh. Technol.* **2014**, *63*, 1581–1592. [CrossRef]
4. Hu, S.; Deng, J.; Mi, C.; Zhang, M. Optimal design of line level control resonant converters in plug-in hybrid electric vehicle battery chargers. *IET Electr. Syst. Transp.* **2013**, *4*, 21–28. [CrossRef]
5. Tan, X.; Ruan, X. Equivalence relations of resonant tanks: A new perspective for selection and design of resonant converters. *IEEE Trans. Ind. Electr.* **2016**, *63*, 2111–2123. [CrossRef]
6. Beiranvand, R.; Rashidian, B.; Zolghadri, M.R.; Alavi, S.M.H. Optimizing the normalized dead-time and maximum switching frequency of a wide-adjustable-range LLC resonant converter. *IEEE Trans. Power Electr.* **2011**, *26*, 462–472. [CrossRef]
7. Beiranvand, R.; Rashidian, B.; Zolghadri, M.R.; Alavi, S.M.H. A design procedure for optimizing the LLC resonant converter as a wide output range voltage source. *IEEE Trans. Power Electr.* **2012**, *27*, 3749–3763. [CrossRef]
8. Fang, X.; Hu, H.; Chen, F.; Somani, U.; Auadisian, E.; Shen, J.; Batarseh, I. Efficiency-oriented optimal design of the LLC resonant converter based on peak gain placement. *IEEE Trans. Power Electr.* **2012**, *28*, 2285–2296. [CrossRef]
9. Hu, S.; Li, X.; Lu, M.; Luan, B.-Y. Operation modes of a secondary-side phase-shifted resonant converter. *Energies* **2015**, *8*, 6098–6113. [CrossRef]
10. Jang, J.; Joung, M.; Choi, S.; Choi, Y.; Choi, B. Current mode control for LLC series resonant DC-to-DC converters. *Energies* **2014**, *14*, 21–27.
11. Han, J.H.; Lim, Y.C.; Sciubba, E. Design of an LLC resonant converter for driving multiple LED lights using current balancing of capacitor and transformer. *Energies* **2015**, *8*, 2125–2144. [CrossRef]
12. Jiang, T.; Zhang, J.; Wu, X.; Sheng, K.; Wang, Y. A bidirectional LLC resonant converter with automatic forward and backward mode transition. *IEEE Trans. Power Electr.* **2014**, *30*, 757–770. [CrossRef]
13. Jiang, T.; Chen, X.; Zhang, J.; Wang, Y. Bidirectional LLC resonant converter for energy storage applications. In Proceedings of the IEEE Applied Power Electronics Conference and Exposition, Long Beach, CA, USA, 17–21 March 2013; pp. 1145–1151.
14. Mu, M.; Lee, F.C. Design and optimization of a 380–12 V high-frequency, high-current LLC converter with GaN devices and planar matrix transformers. *IEEE J. Emerg. Sel. Top. Power Electr.* **2016**, *4*, 854–862.
15. Zhang, W.; Wang, F.; Costinett, D.J.; Tolbert, L.M.; Blalock, B.J. Investigation of gallium nitride devices in high-frequency LLC resonant converters. *IEEE Trans. Power Electr.* **2016**, *2*, 571–583. [CrossRef]
16. Xie, X.; Zhang, J.; Zhao, C.; Zhao, Z.; Qian, Z. Analysis and optimization of LLC resonant converter with a novel over-current protection circuit. *IEEE Trans. Power Electr.* **2007**, *22*, 435–443. [CrossRef]
17. Fei, C.; Lee, F.C.; Li, Q. Digital implementation of soft start-up and short-circuit protection for high-frequency LLC converters with optimal trajectory control (OTC). *IEEE Trans. Power Electr.* **2017**, *32*, 8008–8017. [CrossRef]
18. Jovanović, M.M.; Irving, B.T. On-the-fly topology-morphing control-efficiency optimization method for LLC resonant converters operating in wide input- and/or output-voltage range. *IEEE Trans. Power Electr.* **2015**, *31*, 2596–2608. [CrossRef]
19. Gu, Y.; Lu, Z.; Hang, L.; Qian, Z.; Huang, G. Three-level LLC series resonant DC/DC converter. *IEEE Trans. Power Electr.* **2005**, *20*, 781–789. [CrossRef]
20. Hu, Z.; Qiu, Y.; Wang, L.; Liu, Y.-F. An interleaved LLC resonant converter operating at constant switching frequency. *IEEE Trans. Power Electr.* **2014**, *29*, 2931–2943. [CrossRef]
21. Wu, H.; Xia, T.; Zhan, X.; Xu, P.; Xing, Y. Resonant converter with resonant-voltage-multiplier rectifier and constant-frequency phase-shift control for isolated buck-boost power conversion. *IEEE Trans. Ind. Electr.* **2015**, *62*, 6974–6985. [CrossRef]

22. Inam, W.; Afridi, K.K.; Perreault, D.J. High efficiency resonant DC/DC converter utilizing a resistance compression network. In Proceedings of the IEEE Applied Power Electronics Conference and Exposition, Long Beach, CA, USA, 17–21 March 2013; pp. 1399–1405.
23. Wu, H. Interleaved LLC resonant converter with hybrid rectifier and variable-frequency plus phase-shift control for wide output voltage range applications. *IEEE Trans. Power Electr.* **2017**, *32*, 4246–4257. [CrossRef]
24. Wu, J.; Li, Y.; Sun, X.; Liu, F. A new dual-bridge series resonant DC-DC converter with dual-tank. *IEEE Trans. Power Electr.* **2017**, 1. [CrossRef]
25. Outeiro, M.T.; Buja, G.; Czarkowski, D. Resonant power converters: An overview with multiple elements in the resonant tank network. *IEEE Ind. Electr. Mag.* **2016**, *10*, 21–45. [CrossRef]
26. Hu, H.; Fang, X.; Chen, F.; Shen, Z.J.; Batarseh, I. A modified high-efficiencvy LLC converter with two transformers for wide input-voltage range applications. *IEEE Trans. Power Electr.* **2012**, *28*, 1946–1960. [CrossRef]
27. Liang, Z.; Guo, R.; Li, J.; Huang, A.Q. A high-efficiency PV module-integrated DC/DC converter for PV energy harvest in FREEDM systems. *IEEE Trans. Power Electr.* **2011**, *26*, 897–909. [CrossRef]
28. Hua, C.-C.; Fang, Y.H.; Lin, C.W. LLC resonant converter for electric vehicle battery chargers. *IET Power Electr.* **2016**, *9*, 2369–2376. [CrossRef]
29. Qu, X.; Wong, S.C.; Chi, K.T. An improved LCLC current-source-output multistring LED driver with capacitive current balancing. *IEEE Trans. Power Electr.* **2015**, *30*, 5783–5791. [CrossRef]
30. Wang, Y.; Guan, Y.; Xu, D.; Wang, W. A CLCL resonant DC/DC converter for two-stage LED driver system. *IEEE Trans. Ind. Electr.* **2016**, *63*, 2883–2891. [CrossRef]